Journal of Materials Chemistry C

ROYAL SOCIETY OF CHEMISTRY

PAPER

View Article Online
View Journal | View Issue

Cite this: J. Mater. Chem. C, 2025, 13, 10621

Super-wide-range tunable emission across NIR-II and NIR-III achieved by B-site cation co-substitution in Ni^{2+}-doped double perovskites for NIR light sources†

Yifu Zhuo,[a] Yaping Niu,[a] Fugen Wu,*[b] Jie Li,[a] Yun Wang,[a] Qi Zhang,[cde] Yun Teng,[de] Xiaozhu Xie,[f] Huafeng Dong[g] and Zhongfei Mu*[ah]

Received 12th February 2025,
Accepted 15th April 2025

DOI: 10.1039/d5tc00613a

rsc.li/materials-c

Long-wavelength (1000–2500 nm) near-infrared (LWNIR) phosphors present important application prospects in biomedical and nondestructive testing. A major challenge for current researchers is obtaining phosphors with super-wide-range emission across the NIR-II and NIR-III spectral regions, which is highly advantageous for the development of NIR light sources. Ni^{2+} is a prominent activator for LWNIR emission and is sensitive to the octahedral crystal field environment. Herein, a series of Ni^{2+}-doped $Sr_2B'B''O_6$ (B'^{3+} = Ga, Sc; B''^{5+} = Ta, Sb) phosphors with double perovskite structures was investigated. Through crystal field engineering of B-site cations, specifically Sc^{3+}–Sb^{5+} co-substitution for Ga^{3+}–Ta^{5+}, the emission peak of Ni^{2+} was tuned from 1295 to 1665 nm. Such a super-wide-range tunable emission of up to 370 nm was unprecedented. The emission spectra of $Sr_2Ga_{1-x}Sc_xTa_{1-y}Sb_yO_6$:0.01$Ni^{2+}$ solid solution phosphors ranged from 1000 to 2100 nm (across NIR-II and NIR-III). The excitation peak was correspondingly shifted from 398 to 454 nm, which was suitable for commercial near-ultraviolet and blue LEDs. The potential applications of our phosphors in biomedical imaging and nondestructive testing were demonstrated. This work not only developed an efficient super-wide-range tunable emission phosphor suitable for LWNIR light sources but also revealed the emission characteristics of Ni^{2+}-doped double perovskites, providing important technical guidance for achieving LWNIR emission and developing large-range tunable phosphors.

1. Introduction

In recent decades, near-infrared (NIR) spectroscopy has been widely used in the fields of night vision, anti-counterfeiting, temperature measurement, biological imaging, substance identification, and so on.[1–6] Incandescent and halogen lamps, as traditional NIR light sources, have prominent drawbacks, such as large volume, high operating temperature, low photoelectric conversion efficiency, and short lifetimes. Thus, some researchers have turned their attention to quantum dots, metal halides, and organic polymers.[7–9] However, these materials usually present unavoidable shortcomings, such as low luminous efficiency, poor stability, and untunable emission. Recently developed NIR phosphor-converted light-emitting diodes (pc-LEDs) can effectively overcome these drawbacks, offering advantages such as low cost, high efficiency, long lifetime, and tunable broadband emission.

The activators of NIR phosphors mainly include rare earth metal ions and transition metal ions. Emission from the former is primarily attributed to 4f–4f spin forbidden transitions, which exhibit sharp line emission characteristics, while emission from the latter is broadband due to 3d–3d spin-allowed

[a] School of Materials and Energy, Guangdong University of Technology, Waihuan Xi Road, No. 100, Guangzhou 510006, People's Republic of China. E-mail: muzhongfei@gdut.edu.cn
[b] The College of Information Engineering, Guangzhou Vocational University of Science and Technology, Guangcong Nine Road, Guangzhou, 510550, People's Republic of China. E-mail: wufugen@gkd.edu.cn
[c] The School of Information Engineering, Guangdong University of Technology, Guangzhou 510006, People's Republic of China
[d] The School of Electronic Engineering, Beijing University of Posts and Telecommunications, Bejing100876, People's Republic of China
[e] Beijing Key Laboratory of Space-Ground Interconnection and Convergence, Beijing 100876, People's Republic of China
[f] Laser Micro/Nano Processing Lab, School of Electromechanical Engineering, Guangdong University of Technology, Guangzhou 510006, People's Republic of China
[g] School of Physics and Optoelectronic Engineering, Guangdong University of Technology, Waihuan Xi Road, No. 100, Guangzhou, 510006, People's Republic of China
[h] Department of Experimental Teaching, Guangdong University of Technology, Waihuan Xi Road, No. 100, Guangzhou, 510006, People's Republic of China

† Electronic supplementary information (ESI) available. See DOI: https://doi.org/10.1039/d5tc00613a

transitions. Broadband NIR spectroscopy offers broader application potential because it can cover a larger detection range. So far, there have been numerous investigations on transition metal ion-doped (such as Mn^{2+}, Mn^{4+}, Cr^{3+}, Fe^{3+}) phosphors.[10–13] Among these transition metal ions, Cr^{3+} ions have become a focus of research owing to their strong absorption in the blue light region and super-broadband emission in many hosts, such as La_2MgZrO_6:Cr^{3+}[14] (full width at half maximum (FWHM) = 210 nm), $Mg_7Ga_2GeO_{12}$:Cr^{3+}[15] (FWHM = 226 nm), $Li_3Sc_2(PO_4)_3$:Cr^{3+}[16] (FWHM = 240 nm), and $LaTiTaO_6$:Cr^{3+}[17] (FWHM = 300 nm). Exploration of the NIR emission from non-toxic Fe^{3+} is also rapidly emerging; however, relevant applications are limited because its excitation is mainly located in the ultraviolet range. Examples include $MgGa_2O_4$:Fe^{3+},[18] Sr_2LuSbO_6:Fe^{3+},[19] and $Ca_{2.5}Hf_{2.5}(Ga, Al)_3O_{12}$:$Fe^{3+}$.[20] In addition, NIR emission from transition metal ions is highly sensitive to the surrounding crystal field environment. Luminescence tuning and enhancement can be achieved by constructing chemical unit substitutions in solid solutions to modify the crystal field environment within the host lattice. For example, Liu *et al.*[21] reported $LiIn_2SbO_6$:Cr^{3+} phosphors, and controllable emission tuning from 965 to 892 nm is achieved by chemical unit co-substitution of [Zn^{2+}–Zn^{2+}] for [Li^{+}–In^{3+}]. Zhao *et al.*[22] developed a series of antimonate materials A_2MSbO_6:Cr^{3+} (A^{2+} = Ca, Sr, Ba; M^{3+} = Ga, In, Sc, Y) with double perovskite structure. Through a composition modulation, the NIR emission peaks ranged from 825 to 1010 nm. Zhang *et al.*[23] designed ABO_4:Cr^{3+} (A^{3+} = Ga, Sc, In; B^{5+} = Ta, Nb) NIR emission phosphors based on crystal field engineering. Through cation substitution, spectral tuning of nearly 200 nm (from 825 to 1025 nm) is achieved as the crystal field strength decreases. Moreover, Zhang *et al.*[24] and Liu *et al.*[25] reported the Fe^{3+} activated double perovskite NIR phosphors A_2BSbO_6:Fe^{3+} (A = Ca, Sr, Ba; B = Sc, Y, Ga) and $A_2BB'O_6$:Fe^{3+}(A = Sr^{2+}, Ca^{2+}; B, B′ = In^{3+}, Sb^{5+}, Sn^{4+}). The emission tuning in the range from 842 to 944 nm and from 885 to 1005 nm is achieved by crystal field engineering, respectively.

It is worth noting that emission from the above-mentioned transition metal ions is usually located in the NIR-I (700–1000 nm) region. Meanwhile, the vibration absorption of chemical groups, such as C–H, N–H, and O–H bonds, are located in the long-wavelength near-infrared (LWNIR) regions with longer wavelengths (1000–2500 nm).[26] Therefore, there is an urgent need to develop efficient LWNIR emitting materials. Ni^{2+} with $3d^8$ electrical configuration is an ideal LWNIR emitting activator due to $^3T_{2g}(F) \rightarrow {}^3A_{2g}(F)$ spin-permitted transitions. Similarly, the emission from Ni^{2+} ions is also sensitive to the crystal field environment. Huang *et al.*[27] studied Ca_2GeO_4:Ni^{2+} and found that Ni^{2+} ions can yield sharp emission (FWHM = 16 nm) when entering the [GeO_4] tetrahedron with lower formation energy. However, studies have found that Ni^{2+} ions exhibit broadband emission in octahedral crystal fields, and the FWHM usually exceeds 200 nm.[28–30] At present, one of the main systems for the investigation of Ni^{2+} ions is Cr^{3+} and Ni^{2+} co-doped luminescent materials.[31–35] The aim is to improve the blue light absorption of Ni^{2+} with the help of energy transfer from Cr^{3+} to Ni^{2+}. However, it does not solve the problem of tunable emission of Ni^{2+} ions to cover a larger LWNIR range. For the NIR pc-LEDs, the use of emission tunable phosphors makes it easy to achieve super-wide-range band emission using only a single solid solution phosphor, avoiding the use of multiple phosphors with unavoidable problems, such as differentiated optimal excitation wavelengths, reabsorption between different phosphors, complex preparation processes, and high cost. So far, few investigations have been reported on the tunability of the Ni^{2+} NIR emission. The octahedra in the double perovskite structure provide favorable conditions for the broadband emission of Ni^{2+} ions, and its B site can be flexibly adjusted by cation substitution. As with the Cr^{3+} and Fe^{3+} doped double perovskite structure described earlier, the luminescence tuning of Ni^{2+} in this structure can be expected.

Previous researchers have found that the emission wavelength of phosphors can be effectively tuned either by Sc^{3+} substitution for Ga^{3+} or Sb^{5+} substitution for Ta^{5+}.[36–39] This forms the basis of the current work. We designed and synthesized a series of Ni^{2+} doped $Sr_2B'B''O_6$ (B'^{3+} = Ga, Sc; B''^{5+} = Ta, Sb) phosphors and obtained LWNIR emissions covering 1000–2100 nm across the NIR-II and NIR-III spectral region. When the cations Ga^{3+} and Ta^{5+} at the B sites are gradually substituted by Sc^{3+} and Sb^{5+}, the emission peak is shifted from 1295 to 1665 nm. The super-wide emission tuning range of nearly 370 nm is unprecedented. Simultaneously, the excitation wavelength is also shifted from 398 to 454 nm. A super-wide-range emission with FWHM up to 368 nm of mixing $Sr_2Ga_{1-x}Sc_x$-$Ta_{1-y}Sb_yO_6$:$0.01Ni^{2+}$ solid solution phosphors in equal proportion was presented under the excitation of a 395 nm near-ultraviolet (NUV) chip. In addition, the applications of phosphors in qualitative and quantitative analyses of liquid substances and bioimaging were verified. This study provides an effective strategy for developing long-wavelength, high-efficiency NIR materials and obtaining a super-wide NIR tuning range.

2. Experimental section

2.1 Materials and synthesis

A series of phosphors, including Sr_2GaTaO_6:$X Ni^{2+}$ (X = 0.002, 0.006, 0.01, 0.02, 0.03, 0.04, 0.06), Sr_2GaSbO_6:$0.01Ni^{2+}$ and $Sr_2Ga_{1-x}Sc_xTa_{1-y}Sb_yO_6$:$0.01Ni^{2+}$, (($x$, y) = (0, 0), (0.3, 0), (0.5, 0), (0.7, 0), (1, 0), (1, 0.3), (1, 0.5), (1, 0.7), (1, 1)) solid solution, were synthesized by traditional high-temperature solid-phase method. $SrCO_3$ (99%), Ga_2O_3 (99.999%), Sc_2O_3 (99%), Ta_2O_5 (99.99%), Sb_2O_3 (99.5%), and NiO (99%) were used as raw materials. The raw materials were weighed based on the above-mentioned stoichiometric ratio. H_3BO_3 (99.9%) with a 2% weight percentage was added as flux. An appropriate amount of ethanol was added to mix the raw materials more easily and evenly. These materials were placed into an agate mortar and ground for 30 minutes. The mixed powder was transferred to an alumina crucible and pre-sintered in a muffle furnace at 900 °C for 6 h, then re-sintered at 1300–1450 °C for 8 h. After cooling to room temperature, the obtained powders were reground for further measurements.

2.2 Characterization

The phase composition and crystal structure of the samples were analyzed by X-ray diffraction (XRD, Bruker D8 ADVANCE) with Cu Kα (λ = 1.5406 Å) as the radiation source. XRD Rietveld refinements were performed using FullProf software. The element distribution and surface morphology of the samples were characterized using a scanning electron microscope (SEM, TESCAN MIRA LMS) equipped with an EDS system. High-resolution transmission electron microscopy (HRTEM) and selective area electron diffraction (SAED) images were obtained using JEOL JEM-F200. The X-ray photoelectron spectroscopy (XPS) of the samples was performed using Thermo Scientific K-Alpha. The diffuse reflection (DR) spectra of the samples were measured by a UV-3600 Plus spectrophotometer using $BaSO_4$ as a reference. The Raman spectra of typical samples were recorded with a 532 nm laser using a WITec alpha300R Raman spectrometer. The excitation and emission spectra of the phosphors were monitored by a steady-state fluorescence spectrometer (Edinburgh Instruments FS5), and a temperature control device (MercuryiTC, Oxford) was loaded to obtain temperature-dependent emission spectra using liquid nitrogen as the coolant. The fluorescence attenuation curves, time-resolved photoluminescence (TRPL) spectra and quantum efficiency of typical samples were measured using Edinburgh Instruments FLS1000 fluorescence spectrometer.

2.3 NIR pc-LED device fabrication

The A glue and B glue were weighed based on the mass ratio of 1 : 4. Then, an equal proportion of solid solution phosphors were added to the mixed glue and stirred well for 10 min. The stirred mixture was integrated onto a 395 nm NUV chip and cured in a drying oven at 100 °C for 1 h. The NIR pc-LED device was prepared after complete solidification.

3. Results and discussion

3.1 Structure and composition

Fig. 1(a) shows the crystal structure, lattice parameters and octahedral coordination environment of $Sr_2B'B''O_6$ (B'^{3+} = Ga, Sc; B''^{5+} = Ta, Sb). The octahedra of [$B'O_6$] and [$B''O_6$] form the basic skeleton by alternating links of shared oxygen atoms, and Sr^{2+} ions are accommodated in the void outside the octahedron. Due to the difference in the cation radius at the B site, the structure is distorted in different degrees, resulting in Sr_2GaTaO_6, Sr_2GaSbO_6, Sr_2ScTaO_6 and Sr_2ScSbO_6, belonging to the *I*4/*m*, *I*4/*m*, *P*2$_1$/*c* and *P*12$_1$/*n*1 space groups, respectively. The degree of structural distortion can be preliminarily judged by calculating the tolerance factors through Formula S1 (ESI†).[40] The results show that the Sr_2ScTaO_6 structure has a greater degree of distortion and lower crystal symmetry. From the lattice parameters, it can be found that the lattice expands significantly by Sc^{3+} substitution for Ga^{3+}, while the lattice contracts slightly by Sb^{5+} substitution for Ta^{5+}. The change in lattice distortion and lattice parameters affects the octahedral crystal field environment in the structure, providing effective theoretical support for radiative transitions and emission red-shift of Ni^{2+} ions.

The XRD patterns of the synthesized $Sr_2B'B''O_6$:0.01Ni^{2+} (B'^{3+} = Ga, Sc; B''^{5+} = Ta, Sb) are shown in Fig. 1(b). All the diffraction peaks of the samples are consistent with the corresponding standard cards. The introduction of small amounts of Ni^{2+} does not bring additional phases. This indicates that the designed phosphors have been synthesized successfully. Fig. S1 (ESI†) shows the XRD pattern changes in two alternative routes (first: Sc^{3+} replaces Ga^{3+}, then Sb^{5+} replaces Ta^{5+}; second: Sb^{5+} replaces Ta^{5+}, then Sc^{3+} replaces Ga^{3+}). The deviation of diffraction peaks is caused by the difference in the cation radius. In the six coordinate environment, $R_{Sc^{3+}}$ = 0.75 Å > $R_{Ga^{3+}}$ = 0.62 Å, $R_{Sb^{5+}}$ = 0.60 Å < $R_{Ta^{5+}}$ = 0.64 Å. As a result, the Sc^{3+} substitution for Ga^{3+} causes lattice expansion and shifts the diffraction peak to a smaller angle, while the Sb^{5+} substitution for Ta^{5+} causes lattice contraction and shifts to a larger angle. Rietveld refinement results of solid solution phosphors are shown in Fig. 1(c) and Fig. S2 (ESI†). The values of R_p, R_{wp}, and χ^2 are quite satisfactory, which further indicates the phase purity of the phosphors. The refined crystallographic parameters and main bond lengths are presented in Fig. S3 (ESI†) and Tables S1, S2 (ESI†). As expected, the change in the process of the two groups of samples indicates a significant increase in crystallographic parameters and average bond lengths by Sc^{3+} substitution for Ga^{3+}, while a slight decrease in crystallographic parameters and average bond by Sb^{5+} substitution for Ta^{5+}. This proves the formation of a continuous solid solution. The ionic radius of Ni^{2+} ($R_{Ni^{2+}}$ = 0.69 Å) is similar to Sc^{3+}, Ga^{3+}, Ta^{5+} and Sb^{5+}, and the radius ratio difference (Dr) calculated according to Formula S2 (ESI†) are all less than 30%. There is a significant difference in the valence states between Ni^{2+} and Ta^{5+}/Sb^{5+}. Thus, Ni^{2+} ions are more favorable for entering the [GaO_6] and [ScO_6] octahedra.

Two representative samples, Sr_2GaTaO_6:0.01Ni^{2+} and Sr_2ScSbO_6:0.01Ni^{2+}, were selected to analyze the morphology, composition and valence states. The SEM and EDS images of the two samples are displayed in Fig. 2(a). The samples are composed of 5–10 μm particles, and the elements of Sr, Ga/Sc, Ta/Sb, O, and Ni are uniformly distributed on the surface, demonstrating that Ni^{2+} ions have been doped into the host lattice successfully. Fig. 2(b) shows the HRTEM images of two samples. The interplanar spacings of (112) and ($\bar{1}\bar{1}2$) planes, corresponding to the main diffraction peaks, increase from 2.918 to 2.995 Å, further confirming the lattice expansion caused by Sc^{3+} and Sb^{5+} co-substitution for Ga^{3+} and Ta^{5+}. In addition, the crystal planes corresponding to the two diffraction peaks are distinguished in the SAED image. Fig. S4 (ESI†) shows the XPS full spectra of two samples and the main elements exhibiting a strong signal. The peaks of the Ni fine spectra are relatively weaker in Fig. 2(c) due to the low content in the system. However, there are mainly two peaks corresponding to the 2p$_{3/2}$ and 2p$_{1/2}$ orbitals of Ni, which is consistent with the binding energy of Ni^{2+}.

3.2 Luminescence properties

The DR spectra of four typical samples, undoped and doped, are displayed in Fig. S5 (ESI†). All samples exhibit strong

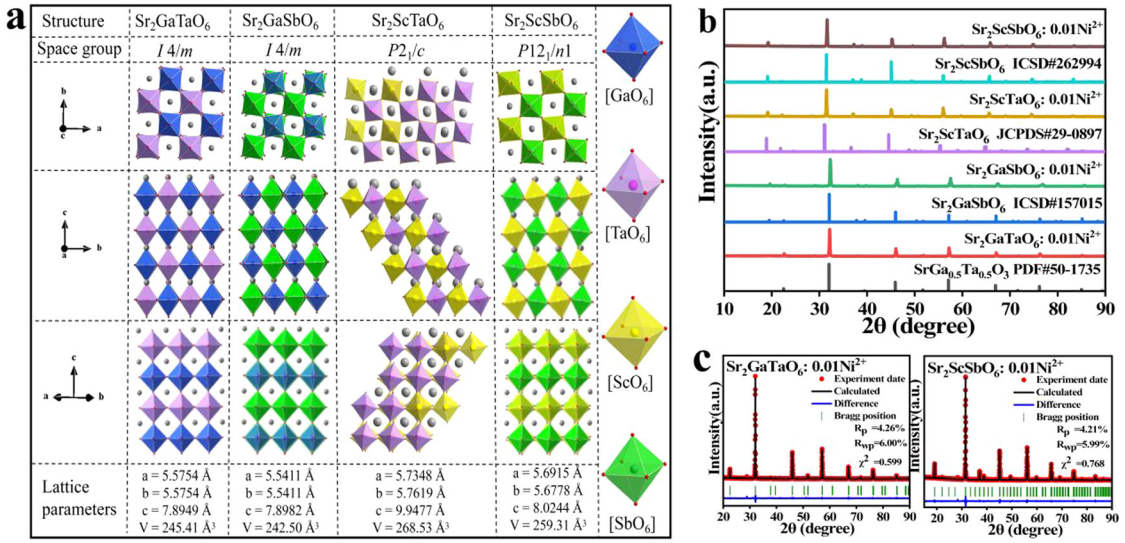

Fig. 1 (a) Crystal structure diagram, lattice parameters, and octahedral coordination environment of $Sr_2B'B''O_6$ (B'^{3+} = Ga, Sc; B''^{5+} = Ta, Sb); (b) XRD patterns of $Sr_2BB'O_6$ (B = Ga, Sc; B′ = Ta, Sb):0.01Ni^{2+}; (c) Rietveld refinement of Sr_2GaTaO_6:0.01Ni^{2+} and Sr_2ScSbO_6:0.01Ni^{2+}.

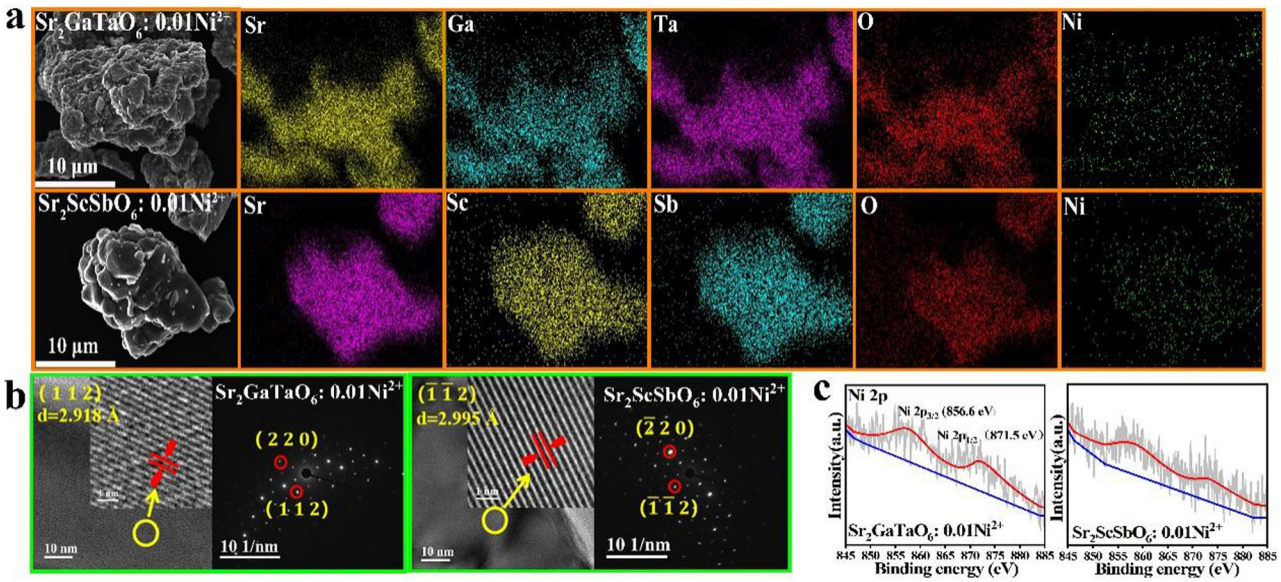

Fig. 2 (a) SEM images and EDS elemental mapping of Sr_2GaTaO_6:0.01Ni^{2+} and Sr_2ScSbO_6:0.01Ni^{2+}; (b) HRTEM and SAED images of Sr_2GaTaO_6:0.01Ni^{2+} and Sr_2ScSbO_6:0.01Ni^{2+}; (c) Ni XPS fine spectra of Sr_2GaTaO_6:0.01Ni^{2+} and Sr_2ScSbO_6:0.01Ni^{2+}.

absorption around 200–350 nm, corresponding to the transition from the valence band to the conduction band of the host materials. Sr_2GaSbO_6 host has a certain degree of absorption form visible to the NIR region, while Sr_2GaTaO_6, Sr_2ScTaO_6, and Sr_2ScSbO_6 hosts do not have significant absorption. This has an important impact on the luminescence of Ni^{2+}. According to the Kubelka–Munk equation (Formula S3 and S4 (ESI†)),[41] the band gap (E_g) values of Sr_2GaTaO_6, Sr_2ScTaO_6, and Sr_2ScSbO_6 are calculated to be 4.46, 4.55, and 4.12 eV, respectively, which are much larger than the 3.38 eV of Sr_2GaSbO_6. Three strong absorption bands and one weak absorption band appear after the incorporation of Ni^{2+}, corresponding to the $^3A_{2g}$ (F) → $^3T_{1g}$ (P), $^3A_{2g}$ (F) → $^1T_{2g}$ (D), $^3A_{2g}$ (F) → $^3T_{1g}$ (F), $^3A_{2g}$ (F) → $^3T_{2g}$ (F) transitions from left to right, respectively.

As illustrated in Fig. 3(a), compared with the original structure Sr_2GaTaO_6:0.01Ni^{2+}, four absorption bands present a significant red-shift trend by Sc^{3+} substitution for Ga^{3+} and Sb^{5+} substitution for Ta^{5+}. This indicates that the 3d orbital crystal field environment of Ni^{2+} is strongly affected by ion substitution engineering. The effect of doping amount on the photoluminescence performance of the initial structure is exhibited in Fig. 3(b). The broadband emission from 1000 to

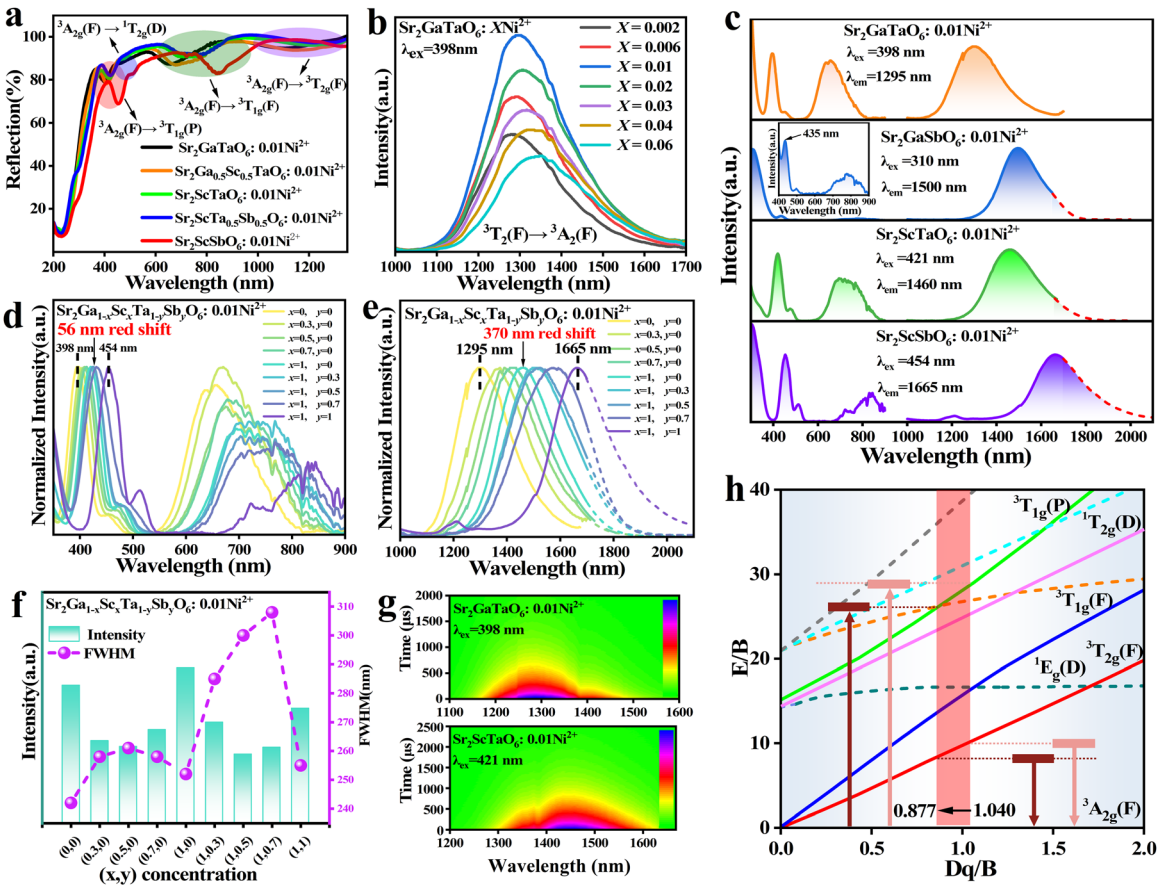

Fig. 3 (a) DR spectra of representative solid solution phosphors; (b) concentration-dependent emission spectra of Sr_2GaTaO_6:XNi^{2+} under excitation at 398 nm; (c) excitation and emission spectra of $Sr_2B'B''O_6$:0.01Ni^{2+} (B′$^{3+}$ = Ga, Sc; B″$^{5+}$ = Ta, Sb) phosphors; (d) normalized excitation spectra of $Sr_2Ga_{1-x}Sc_xTa_{1-y}Sb_yO_6$:0.01Ni^{2+} solid solution phosphors; (e) normalized emission spectra of $Sr_2Ga_{1-x}Sc_xTa_{1-y}Sb_yO_6$:0.01Ni^{2+} solid solution phosphors; (f) change in emission intensity and FWHM of $Sr_2Ga_{1-x}Sc_xTa_{1-y}Sb_yO_6$:0.01Ni^{2+} solid solution phosphors; (g) TRPL mapping of Sr_2GaTaO_6:0.01Ni^{2+} and Sr_2ScTaO_6:0.01Ni^{2+}. (h) Tanabe–Sugano diagram of Ni^{2+} in the octahedral crystal field.

1700 nm is exhibited in Sr_2GaTaO_6:XNi^{2+} phosphors under the 398 nm excitation, which is attributed to the $^3T_{2g}$ (F) → $^3A_{2g}$ (F) transition of Ni^{2+}. With the increase in Ni^{2+} doping concentration, the luminous intensity increases first, then decreases, and the optimal luminous intensity is obtained when X = 0.01, where the emission peak is located at 1295 nm. It can be observed that the emission peak position is red-shifted with the continuous introduction of Ni^{2+}. This is attributed to the enhanced interaction of the exchange coupled Ni^{2+}–Ni^{2+} ion pairs, which leads to the energy level splitting of the excited state, reducing the energy difference between $^3T_{2g}$(F) and $^3A_{2g}$(F).[42]

In order to explore the change in luminescence properties by Sc^{3+} substitution for Ga^{3+} and Sb^{5+} substitution for Ta^{5+}, the excitation and emission spectra of $Sr_2B'B''O_6$:0.01Ni^{2+} (B′$^{3+}$ = Ga, Sc; B″$^{5+}$ = Ta, Sb) phosphors are depicted in Fig. 3(c) (the dashed line is the result of curve fitting owing to the testing range of the detector). Similar to the DR spectra, three characteristic excitation peaks of Ni^{2+} are all exhibited in the excitation spectra of four samples, and the excitation band of 300–350 nm is caused by the interband transition between the valence band and the conduction band. Significantly, the peak wavelengths of excitation and emission spectra of Ni^{2+} are changed by adjusting the cation composition. For Sr_2ScTaO_6: 0.01Ni^{2+}, the excitation and emission peaks are located at 421 and 1460 nm, respectively. For Sr_2ScSbO_6:0.01Ni^{2+}, the excitation and emission peaks are located at 454 and 1665 nm, respectively. Owing to the strong absorption in the DR spectrum and low E_g value of Sr_2GaSbO_6:0.01Ni^{2+}, the characteristic excitation and emission of Ni^{2+} are relatively weak. Localized amplification was performed on the characteristic excitation of Ni^{2+}. For Sr_2GaSbO_6:0.01Ni^{2+}, and the excitation and emission peaks are located at 435 and 1500 nm, respectively. In an effort to study the spectral change before and after substitution in more detail, $Sr_2Ga_{1-x}Sc_xTa_{1-y}Sb_yO_6$:0.01Ni^{2+} solid solution phosphors were selected for analysis. All samples are pure phase (Fig. S6, ESI†). The normalized excitation and emission spectra of solid solution phosphors are presented in Fig. 3(d) and (e). With the increase in x value (Ga^{3+} is gradually substituted by Sc^{3+}), the excitation and emission spectra were gradually red-shifted. After complete substitution, the excitation spectra show a red-shift from 398 to 421 nm, and the emission spectra show a red-shift from 1295 to 1460 nm. Similarly, with the increase in the y value (Ta^{5+} is gradually

substituted by Sb^{5+}), the excitation spectra show a further red-shift from 421 to 454 nm, and the emission spectra show a further red-shift from 1460 to 1665 nm. The results show that Ga^{3+} and Ta^{5+} are gradually substituted by Sc^{3+} and Sb^{5+} in Ni^{2+} doped $Sr_2Ga_{1-x}Sc_xTa_{1-y}Sb_yO_6$ solid solution, and the emission peak causes an enormous red-shift of 370 nm, which is unprecedented. The entire emission range covers 1000–2100 nm, which realizes the super-wide-range emission across the NIR-II and NIR-III regions. Such a large spectral response range demonstrates it is suitable for LWNIR light sources and has an extensive application prospect. Furthermore, the excitation peak shifts from 398 (NUV) to 454 nm (blue), which better matches the current highly commercialized NUV and blue LED chips, further highlighting its application potential. Both luminous intensity and FWHM change with increasing substitution, as depicted in Fig. 3(f). It can be observed that a higher luminous intensity can be obtained when the B sites are completely occupied by one type of cation. The luminous intensity decreases and the FWHM increases accordingly in the intermediate solid solution. That might be due to the lattice distortions and defects caused by the difference in ionic radius during the substitution process. These distortions and defects can result in the enhancement of phonon scattering, and the stronger electron–phonon coupling (EPC) effect increases the non-radiative transition of Ni^{2+} ions. Among them, Sr_2ScTaO_6:$0.01Ni^{2+}$ phosphor has the highest emission intensity, followed by Sr_2GaTaO_6:$0.01Ni^{2+}$ and Sr_2ScSbO_6:$0.01Ni^{2+}$. Generally, an increase in Stokes shift will reduce the emission intensity. Nevertheless, researchers have shown that crystal symmetry also has an effect on luminous intensity.[21,43–45] The reduction of symmetry is beneficial for breaking the forbidden transition of Ni^{2+}, thereby enhancing luminescence. The Raman spectra of three samples are presented in Fig. S7 (ESI†). Multiple vibrational stretches of 50–210 cm^{-1} are assigned to the Sr–O polyhedra, while vibrational stretches of 400–480 cm^{-1} and 730–930 cm^{-1} are attributed to the $[B'O_6]$ and $[B''O_6]$ octahedra, respectively. The shift of Raman peaks to lower wave numbers is related to the bond length changes before and after substitution.[24,25,39,46] Generally, the stronger the chemical bond, the higher the corresponding molecular vibration frequency. It can be clearly seen that the Raman peaks of Sr_2ScTaO_6:$0.01Ni^{2+}$ are more split and sharper, indicating that its internal structure exhibits lower symmetry. In order to investigate the sites occupied by Ni^{2+} doping, two samples of Sr_2GaTaO_6:$0.01Ni^{2+}$ and Sr_2ScTaO_6:$0.01Ni^{2+}$ were selected for analysis. The emission spectra of the two samples were tested at 77 and 298 K (Fig. S8, ESI†). The results show that the asymmetry of the spectral profile is more obvious at low temperatures. An asymmetric spectrum may indicate the presence of multiple luminescent centers. However, the excitation spectra and fluorescence attenuation curves of the two samples monitored at different wavelengths are almost identical. Additionally, TRPL testing is shown in Fig. 3(g). (the slight change in intensity around 1380 nm is caused by the instrument). TRPL mapping shows a single luminous center and a uniform attenuation trend. A similar phenomenon exists in Sr_2ScSbO_6:Fe^{3+},[24] Ca_2InSbO_6:Fe^{3+},[25] and $CaLaMgSbO_6$:Ni^{2+}.[47] These results imply that Ni^{2+} is highly likely to occupy the Ga^{3+}/Sc^{3+} sites.

The emission region of Ni^{2+} is closely related to the octahedral crystal field environment. The crystal field strength of Ni^{2+} in the octahedron can be described by the Tanabe–Sugano theory. The crystal field strength Dq and Racah parameter B can be calculated by the Formula (S5) and (S6) (ESI†).[48] The Tanabe–Sugano energy level diagram in Fig. 3(h) can be used to represent the $3d^8$ energy level splitting of Ni^{2+}. Dq/B is the crystal field parameter, and the strong or weak crystal field is distinguished by the Dq/B value ($\approx$1.75) corresponding to the intersection of $^3T_{2g}$(F) and ^1E_g(D) energy levels. The average bond length, degree of $[(Ga/Sc)O_6]$ octahedral distortion, crystal field parameters, and the corresponding excitation and emission wavelength of representative solid solution phosphors are listed in Table 1. The Dq/B value decreases from 1.040 to 0.877, indicating that Ni^{2+} is in a weak crystal field environment and presents a broadband emission. Different crystal field parameters correspond to different energy values, and the $^3T_{1g}$(P) excited state is much higher than the $^3T_{2g}$(F) excited state and the $^3A_{2g}$(F) ground state. The substitution engineering causes a gradual decrease in Dq/B, and both of the required energy decreases for electrons to transition from the $^3A_{2g}$(F) ground state to the $^3T_{1g}$(P) excited state and return from the $^3T_{2g}$ (F) excited state to the $^3A_{2g}$(F) ground state. As a result, the excitation and emission spectra of phosphors show a red-shift phenomenon. Under the same condition, the crystal field strength Dq is inversely proportional to the bond length of the metal–oxygen ligand (Formula S7 (ESI†)).[49] The ionic radius of Sc^{3+} is much larger than that of Ga^{3+}. With the process of ion substitution, the lattice expansion causes the average bond length of Sc–O to be significantly larger than that of Ga–O. Moreover, the nephelauxetic effect has a significant impact on Racah parameter B and is negatively correlated with ionic electronegativity.[50,51] The electronegativity of Sc (1.35) is less than that of Ga (1.81), resulting in a decrease in the average

Table 1 The average bond length, octahedral distortion, crystal field parameters, and corresponding excitation and emission wavelengths of representative solid solution phosphors

Sample	D_{ave} (Ga/Sc–O)	D_{ave} (Ta/Sb–O)	D_{dis} $[(Ga/Sc)O_6]$	Dq (cm^{-1})	B (nm^{-1})	Dq/B	λ_{ex} (nm)	λ_{em} (nm)	FWHM (nm)
Sr_2GaTaO_6:$0.01Ni^{2+}$	1.97825	1.979	0.0024	896.9	862.0	1.040	398	1295	242
$Sr_2Ga_{0.5}Sc_{0.5}TaO_6$:$0.01Ni^{2+}$	2.0431	1.9861	0.0232	862.1	851.6	1.012	409	1390	261
Sr_2ScTaO_6:$0.01Ni^{2+}$	2.0593	2.0186	0.0377	819.7	848.1	0.966	421	1460	252
$Sr_2ScTa_{0.5}Sb_{0.5}O_6$:$0.01Ni^{2+}$	2.0643	2.0177	0.0419	781.3	874.8	0.893	425	1520	$\approx$300
Sr_2ScSbO_6:$0.01Ni^{2+}$	2.069	2.0113	0.0567	724.6	826.4	0.877	454	1665	$\approx$255

cation electronegativity after substitution. The combined effect of factors causes a decrease in the crystal field parameters after Sc^{3+} substitution for Ga^{3+}, resulting in the emission red-shift of Ni^{2+}. For Sb^{5+} substitution Ta^{5+}, Sb^{5+} has a slightly smaller ionic radius than Ta^{5+}, but they have a significant difference in electronegativity (Sb: 2.05; Ta: 1.5). We speculate that the introduction of Sb^{5+} causes strong attraction to the surrounding oxygen ion ligands, making the average bond length of Sb–O smaller than that of Ta–O. The adjacent [ScO_6] octahedron shows a trend of twisting and stretching. With an increase in the Sc–O bond length, the emission of Ni^{2+} presents a further red-shift. Besides the above effects, the crystal field splitting is enhanced with the degree of octahedral distortion; the distortion of [(Ga/Sc)O_6] can be expressed by the Formula (S8) (ESI†).[52] With the substitution of Sc^{3+} and Sb^{5+}, the distortion degree of [(Ga/Sc)O_6] octahedron continues to increase, causing a larger crystal field splitting to reduce the emission energy. These results illustrate that the change in host components can markedly influence the crystal field environment, thereby affecting the luminescence efficiency and emission peak position of the doped ions. These properties provide an idea for Ni^{2+} emission tuning, which is expected to achieve higher quantum efficiency and longer wavelength emission of LWNIR phosphors by changing the composition of the host.

3.3 Luminous thermal stability

Temperature has a prominent influence on the luminescence properties of phosphors. The temperature-dependent luminescence characteristics of Sr_2GaTaO_6:0.01Ni^{2+}, Sr_2ScTaO_6:0.01Ni^{2+}, and Sr_2ScSbO_6:0.01Ni^{2+} were studied. Fig. S9 (ESI†) exhibits the temperature-dependent emission spectra of the three samples in the 80–455 K range. The temperature-dependent contour plots are shown in Fig. 4(a). As the temperature increases, the emission intensity of all samples decreases due to an increase in non-radiative transitions caused by lattice thermal vibrations. Fig. 4(b) shows the trend of the comprehensive emission intensity of phosphors as a function of temperature. The emission intensity of phosphors changes slightly at low temperatures, while the temperature quenching effect is more serious at high temperatures. Sr_2GaTaO_6:0.01Ni^{2+} shows better luminous thermal stability. At 373 K, the emission intensity of Sr_2GaTaO_6:0.01Ni^{2+} retains 68% of the value at room temperature. However, for Sr_2ScTaO_6:0.01Ni^{2+} and Sr_2ScSbO_6:0.01Ni^{2+}, only 46% and 44% can be maintained. The thermal quenching process can be understood more easily by the configuration coordinate diagram in Fig. 4(c). Electrons are excited from the ground state $^3A_2$ to the excited state $^3T_1$, then relax to the lowest excited state $^3T_2$, returning to the ground state $^3A_2$ by radiative and non-radiative transitions. During this process, the larger the activation energy ΔE, the higher the energy barrier that electrons need to overcome, which reduces the non-radiative transitions and makes the phosphor exhibit high thermal stability of luminescence. The activation energy ΔE can be calculated using the Arrhenius equation (Formula S9 (ESI†)).[53] The thermal activation energy ΔE of the three samples is calculated as 0.232, 0.166 and 0.132 eV, respectively. The decrease in

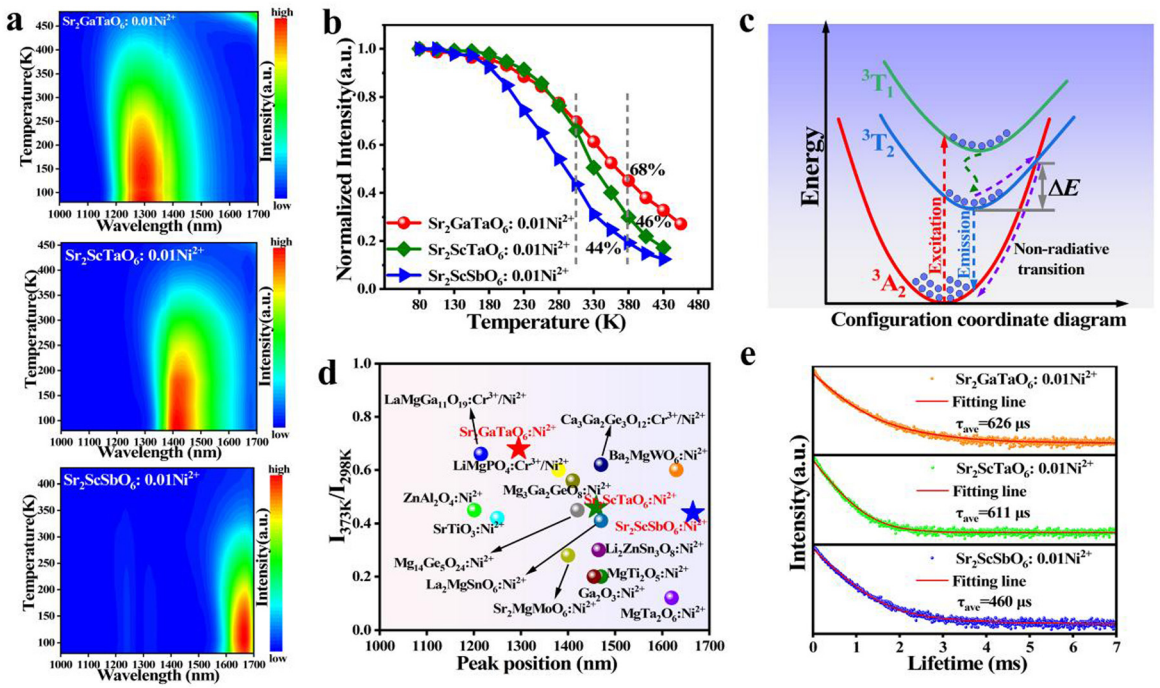

Fig. 4 (a) Temperature-dependent luminescence characteristics contour plot of Sr_2GaTaO_6:0.01Ni^{2+}, Sr_2ScTaO_6:0.01Ni^{2+}, and Sr_2ScSbO_6:0.01Ni^{2+}; (b) the trend of the comprehensive emission intensity of phosphor samples as a function of temperature; (c) Ni^{2+} luminous thermal quenching configuration coordinate curve; (d) luminous thermal stability of Ni^{2+}-doped phosphors; (e) fluorescence attenuation curves of the three samples at room temperature.

activation energy ΔE further verifies that the luminous thermal stability of phosphors is decreasing.

It can be observed that as the temperature increases, the FWHM of the phosphors gradually increases (Fig. S10 (ESI†)). This is related to the strength of the EPC effect inside the crystal material. The EPC strength can be assessed by the changes in FWHM (Formula S10 (ESI†)).[17] The calculated S values for Sr_2GaTaO_6:0.01Ni^{2+} and Sr_2ScTaO_6:0.01Ni^{2+} are 3.098 and 7.134, respectively. Generally, the activation energy depends on the strength of the EPC. In materials with weaker EPC strength, electrons returning to the ground state through non-radiative transition will overcome higher energy barriers and exhibit better luminous thermal stability.[54] Meanwhile, the strong EPC leads to a larger Stokes shift and FWHM, resulting in more serious thermal quenching. EPC also reflects the dependence of thermal stability on structural rigidity. Materials with shorter bond lengths show better structural rigidity, which is conducive to improving the luminous thermal stability of phosphors.[55] Therefore, the selection of the host structure cations is crucial for obtaining high performance LWNIR phosphors. The thermal stability values (I_{373K}/I_{298K}) of Ni^{2+} doped phosphors were investigated and are shown in Fig. 4(d). Our designed phosphors have advantages in thermal stability among the Ni^{2+} doped phosphors. Fig. 4(e) presents the fluorescence attenuation curves of three samples at room temperature. The attenuation curves of all samples can be better fitted by double exponents, possibly due to charge imbalance caused by Ni^{2+} doping, which leads to the existence of defect induced non-radiative transition attenuation paths in the crystals. The fluorescence lifetime can be calculated by the Formula S11 and S12 (ESI†).[56] The average fluorescence lifetime of the three samples is 626, 613 and 460 μs, respectively. The substitution of Sc^{3+} and Sb^{5+} gradually increases the Stokes shift and decreases the fluorescence lifetime. Internal quantum efficiency (IQE) is also an essential factor in evaluating the luminescence properties of phosphors. The IQE measurements of Sr_2GaTaO_6:0.01Ni^{2+}, Sr_2ScTaO_6:0.01Ni^{2+} and Sr_2ScSbO_6:0.01Ni^{2+} are displayed in Fig. S11 (ESI†) and evaluated as 25.6%, 22.3% and 34%, respectively. The comparison of Ni^{2+} doped phosphors in this work and previously reported phosphors is shown in Table 2. It can be deduced that the titled phosphors present greater advantages in luminous region and performance.

3.4 Application prospects

The vibrational overtones of chemical bonds (O–H, C–H, S–H, and N–H) can be perceived through NIR light, and the schematic diagram is illustrated in Fig. 5(a). Different solutions are loaded into the cuvettes, the phosphors are excited by the light source to produce NIR light and pass through the solution, and the transmission spectra data are collected and presented on the screen. The phosphors of Sr_2GaTaO_6:0.01Ni^{2+} and Sr_2ScTaO_6:0.01Ni^{2+} were selected for testing water (H_2O), ammonia ($NH_3\cdot H_2O$), ethanol (C_2H_5OH), acetone (C_3H_6O), and *n*-hexane (C_6H_{14}), respectively, and the results are shown in Fig. 5(b). It can be observed that there are significant differences in the transmission spectra when the NIR light passes through different solutions. The categories and quantities of functional groups and chemical bonds in liquid molecules can affect the absorption of NIR light, enabling qualitative analysis of liquid substances. In addition, even if the absorption peak of the same substance is fixed, there is still a certain degree of difference in the transmission spectra profile owing to the different emission regions of the two phosphors. For example, the absorption of C_3H_6O decreases after 1400 nm, and the transmission increases, while the variation of the emission regions in Sr_2GaTaO_6:0.01Ni^{2+} and Sr_2ScTaO_6:0.01Ni^{2+} cause in different transmission spectra profiles. Based on the difference in the transmission spectra profiles generated by the above two phenomena, the proportion of the two mixed liquids can be determined. The transmission spectra of different H_2O and C_2H_5OH contents were determined by Sr_2GaTaO_6:0.01Ni^{2+} and are presented in Fig. 5(c). With the increase in the proportion of C_2H_5OH, the absorption of the mixed solution gradually turns weak. The relationship between concentration and intensity can be reflected by Lambert–Beer law (Formula S13 (ESI†)).[67] Simultaneously, the wavelength corresponding to the peak of the transmission spectra has also changed. Fig. 5(d) shows the linear fitting results of the changes in transmission intensity and peak wavelength. The excellent fitting results prove that the transmission spectra can accurately reflect the concentration of

Table 2 Comparison of Ni^{2+}-doped phosphors in this study with those of previously reported phosphors

Phosphors	λ_{ex} (nm)	λ_{em} (nm)	Emission (nm)	FWHM (nm)	$I_{373\ K}$ (%)	IQE (%)	Ref.
$SrTiO_3$:Ni^{2+}	365	1250	1000–1600	220	≈55	7.9	57
$ZnAl_2O_4$:Ni^{2+}	365	1251	1000–1600	232	50	—	58
$Mg_3Ga_2GeO_8$:Ni^{2+}	395	1410	1100–1700	300	52.7	36.7	48
Ga_2O_3:Ni^{2+}	410	1455	1100–1700	298	19.2	31.2	59
$MgAl_2O_4$:Ni^{2+}	390	1230	900–1600	251	≈30	18.8	60
$MgTi_2O_5$:Ni^{2+}	395	1470	1200–1700	245	20	23.7	61
$Mg_{14}Ge_5O_{24}$:Ni^{2+}	418	1430	1100–1700	278	≈60	38.5	62
$MgTa_2O_6$:Ni^{2+}	470	1620	1300–2000	—	≈10	25.62	63
La_2MgSnO_6:Ni^{2+}	425	1470	1200–1800	250	≈45	—	64
Ba_2MgWO_6:Ni^{2+}	365	1630	1200–2000	255	≈70	16.67	65
Sr_2MgMoO_6:Ni^{2+}	400	1400	1100–2000	—	26	39.78	66
Ba_2MgMoO_6:Ni^{2+}	400	1610	1200–2000	—	22	21.75	66
Sr_2GaTaO_6:Ni^{2+}	398	1295	1000–1700	242	68	25.6	This work
Sr_2ScTaO_6:Ni^{2+}	421	1460	1100–1900	252	46	22.3	This work
Sr_2ScSbO_6:Ni^{2+}	454	1665	1100–2100	—	44	≈34	This work

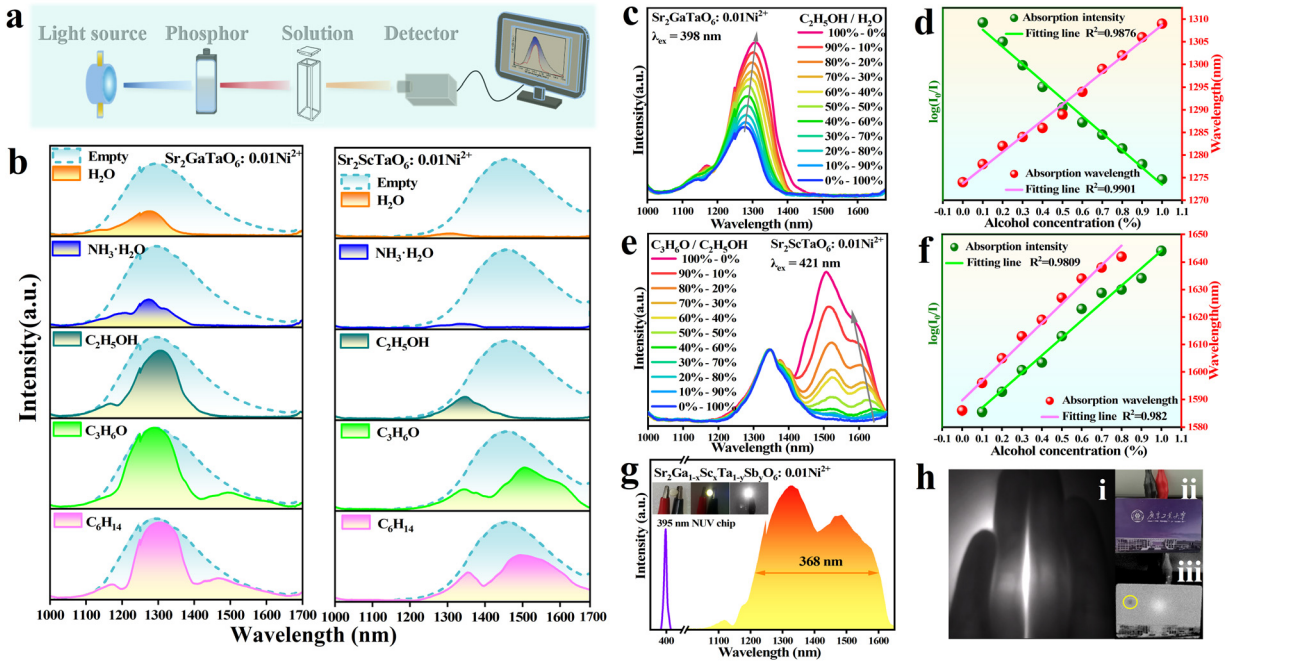

Fig. 5 (a) Schematic of the NIR absorption of liquid substances; (b) transmission spectra of different liquids tested by Sr_2GaTaO_6:0.01Ni^{2+} and Sr_2ScTaO_6:0.01Ni^{2+}; (c) transmission spectra of different H_2O and C_2H_5OH contents tested by Sr_2GaTaO_6:0.01Ni^{2+}; (d) linear fitting results of transmission intensity and peak wavelength for different H_2O and C_2H_5OH contents; (e) transmission spectra of different C_3H_6O and C_2H_5OH contents tested by Sr_2ScTaO_6:0.01Ni^{2+}; (f) linear fitting results of transmission intensity and peak wavelength for different C_3H_6O and C_2H_5OH contents; (g) emission spectra of $Sr_2Ga_{1-x}Sc_xTa_{1-y}Sb_yO_6$:0.01$Ni^{2+}$ phosphors mixed in equal proportions, excited by a 395 nm chip; (h) application of the pc-LED in biological imaging and night vision.

the mixed solution, achieving qualitative analysis of the mixture. Moreover, the determination of different C_3H_6O and C_2H_5OH contents by Sr_2ScTaO_6:0.01Ni^{2+} has also been confirmed, as exhibited in Fig. 5(e) and (f).

In order to verify further applications of phosphors, $Sr_2Ga_{1-x}Sc_xTa_{1-y}Sb_yO_6$:0.01$Ni^{2+}$ solid solution phosphors were mixed in equal proportion and integrated into a 395 nm NUV chip. As illustrated in Fig. 5(g), the spectrum with FWHM up to 368 nm is displayed, covering almost the entire NIR-II region (the abnormal intensity at 1400 nm is caused by the absorption of A glue and B glue). Such a wide spectral range is extremely rare. The photos in the illustration express the conditions without and with current taking under a normal camera or NIR camera. Fig. 5(h) shows a photo of NIR light passing through a finger captured by the NIR camera. The clear blood vessel image highlights its application in biological imaging. Moreover, the location of the campus card chip can be accurately reflected by the NIR camera. The series of results prove that our phosphors present very broad application prospects.

4. Conclusions

In this work, a series of Ni^{2+} doped $Sr_2B'B''O_6$ (B'^{3+} = Ga, Sc; B''^{5+} = Ta, Sb) phosphors with double perovskite structures were synthesized and investigated. Utilizing the flexibility and compatibility of the double perovskite structure through the crystal field engineering of B-site cations, combination Sc^{3+}–Sb^{5+} gradually substitutes Ga^{3+}–Ta^{5+}, and the emission of Ni^{2+} ions cover an extremely broad region from 1000 to 2100 nm across NIR-II and NIR-III. The emission peak is red-shifted from 1295 to 1665 nm with a super-wide tunable range of 370 nm. The excitation peak is also red-shifted from 398 to 454 nm. The synthesized phosphors present desirable luminous efficiency and luminous thermal stability. Besides, the FWHM up to 368 nm can be generated under the excitation of a 395 nm NUV chip by mixing the solid solution phosphors. Meanwhile, the applications of phosphors in liquid qualitative and quantitative analysis, as well as in biological vascular imaging, were demonstrated. This work proves that the Ni^{2+} doped double perovskite phosphors can achieve super-wide-range LWNIR emission tuning, which has an important reference significance for the research and development of NIR-II and NIR-III emitting phosphors.

Data availability

The data supporting the findings of this study are available from the corresponding author upon reasonable request.

Conflicts of interest

The authors declare no conflicts of interest.

Acknowledgements

This work was supported by the National Natural Science Foundation of China (grant no. 52272142, 62127816). The authors also thank the test support from the Shiyanjia Lab (**https://www.shiyanjia.com**).

References

1 W. T. Huang, K. C. Chen, M. H. Huang and R. S. Liu, *Adv. Opt. Mater.*, 2023, **11**, 2301166.
2 M. Li, Y. Jin, L. Yuan, B. Wang, H. Wu, Y. Hu and F. Wang, *ACS Appl. Mater. Interfaces*, 2023, **15**, 13186–13194.
3 Y. Wang, G. Liu and Z. Xia, *Laser Photonics Rev.*, 2024, **18**, 2300717.
4 G. Zhou, Y. Wang, Y. Mao, C. Guo, J. Zhang, M. S. Molokeev, Z. Xia and X. M. Zhang, *Adv. Funct. Mater.*, 2024, **34**, 2401860.
5 Q. Ren, G. Zhou, Y. Mao, N. Zhang, J. Zhang and X. M. Zhang, *Chem. Sci.*, 2024, **15**, 16536–16545.
6 Y. Niu, F. Wu, Q. zhang, Y. Teng, Y. Huang, Z. Yang and Z. Mu, *J. Lumin.*, 2024, **275**, 120748.
7 R. Zhou, J. Xu, P. Luo, L. Hu, X. Pan, J. Xu, Y. Jiang and L. Wang, *Adv. Energy Mater.*, 2021, **11**, 2101923.
8 G. Zhou, Y. Mao, J. Zhang, Q. Ren, M. S. Molokeev, Z. Xia and X. M. Zhang, *Adv. Funct. Mater.*, 2024, **35**, 2413524.
9 Z. Deng, J. Zhang, J. Zhou, W. Shen, Y. Zuo, J. Wang, S. Yang, J. Liu, Y. Chen, C. C. Chen, G. Jia, P. Alam, J. W. Y. Lam and B. Z. Tang, *Adv. Mater.*, 2024, **36**, 2311384.
10 J. X. Du, S. Q. Liu, Z. Song and Q. L. Liu, *ACS Appl. Mater. Interfaces*, 2023, **15**, 53738–53745.
11 Y. Q. Tang, Y. Y. Cai, K. P. Dou, J. Q. Chang, W. Li, S. S. Wang, M. Z. Sun, B. L. Huang, X. F. Liu, J. R. Qiu, L. Zhou, M. M. Wu and J. C. Zhang, *Nat. Commun.*, 2024, **15**, 3209.
12 S. Q. Liu, Y. T. Zheng, D. F. Peng, J. Zhao, Z. Song and Q. L. Liu, *Adv. Funct. Mater.*, 2023, **33**, 2209275.
13 Y. Ye, Y. Ding, H. Yang, Q. Mao, L. Pei, M. Liu and J. Zhong, *Adv. Funct. Mater.*, 2024, **34**, 2405048.
14 H. Zeng, T. Zhou, L. Wang and R. J. Xie, *Chem. Mater.*, 2019, **31**, 5245–5253.
15 J. Xiang, X. Zhou, X. Zhao, Z. Wu, C. Chen, X. Zhou and C. Guo, *Laser Photonics Rev.*, 2023, **17**, 2200965.
16 S. Zhao, L. Lou, S. Yuan, D. Zhu, F. Wu and Z. Mu, *J. Lumin.*, 2022, **251**, 119188.
17 Y. Yang, Z. Lu, H. Fan, M. Chen, L. Shen, X. Zhang, Q. Pang, J. Chen, P. Chen and L. Zhou, *Inorg. Chem.*, 2023, **62**, 3601–3608.
18 Y. Ye, H. Yang, L. Liang, Q. Mao, F. Zhao, Y. Zhu, M. Liu and J. Zhong, *Laser Photon. Rev.*, 2025, **19**, 2400966.
19 J. Y. Su, R. Pang, T. Tan, S. W. Wang, X. X. Chen, S. Zhang and H. J. Zhang, *Adv. Opt. Mater.*, 2024, **12**, 2303187.
20 L. Yan, G. Zhu, S. Ma, S. Li, Z. Li, X. Luo and B. Dong, *Laser Photonics Rev.*, 2024, **18**, 2301200.
21 D. Liu, G. Li, P. Dang, Q. Zhang, Y. Wei, H. Lian, M. Shang, C. C. Lin and J. Lin, *Angew. Chem., Int. Ed.*, 2021, **60**, 14644–14649.
22 M. Zhao, S. Liu, H. Cai, F. Zhao, Z. Song and Q. Liu, *Inorg. Chem. Front.*, 2022, **9**, 4602–4607.
23 Q. Zhang, D. Liu, P. Dang, H. Lian, G. Li and J. Lin, *Laser Photonics Rev.*, 2022, **16**, 2100459.
24 X. Zhang, X. Wu, Y. Xu, S. Yin, C. Zhong, L. Zhou and H. You, *Adv. Opt. Mater.*, 2024, **12**, 2302300.
25 D. Liu, G. Li, P. Dang, Q. Zhang, Y. Wei, L. Qiu, M. S. Molokeev, H. Lian, M. Shang and J. Lin, *Light: Sci. Appl.*, 2022, **11**, 112.
26 S. Yuan, Z. Mu, L. Lou, S. Zhao, D. Zhu and F. Wu, *Ceram. Int.*, 2022, **48**, 26884–26893.
27 W. Huang, J. Zhang, J. Fan, P. Chen, Q. Pang, L. Zhou, Z. C. Wu, Y. Hu and X. Zhang, *Inorg. Chem.*, 2023, **62**, 13370–13377.
28 L. Yuan, Y. Jin, D. Zhu, Z. Mou, G. Xie and Y. Hu, *ACS Sustainable Chem. Eng.*, 2020, **8**, 6543–6550.
29 B. M. Liu, S. M. Gu, L. Huang, R. F. Zhou, Z. Zhou, C. G. Ma, R. Zou and J. Wang, *Cell Rep. Phys. Sci.*, 2022, **3**, 101078.
30 J. Li, C. Wang, Y. Niu, Y. Wang, F. Wu, Z. Qi, Y. Teng, H. Dong and Z. Mu, *Ceram. Int.*, 2024, **50**, 18647–18654.
31 F. Zhao, Y. Shao, Q. Liu and J. Zhong, *Laser Photonics Rev.*, 2024, **18**, 2400447.
32 Q. Zhang, G. Li, G. Li, D. Liu, P. Dang, L. Qiu, H. Lian, M. S. Molokeev and J. Lin, *Adv. Opt. Mater.*, 2024, **12**, 2301429.
33 C. Wang, Y. Niu, Y. Wang, F. Wu, Q. Zhang, Y. Teng, H. Dong and Z. Mu, *Inorg. Chem.*, 2024, **63**, 14383–14391.
34 Z. Gao, Y. Zhang, Y. Li, S. Zhao, P. Zhang, X. Dong, D. Deng and S. Xu, *Inorg. Chem. Front.*, 2024, **11**, 4711–4720.
35 Y. Zhuo, F. Wu, Y. Niu, Y. Wang, Q. zhang, Y. Teng, H. Dong and Z. Mu, *Laser Photonics Rev.*, 2024, **18**, 2400105.
36 J. Fan, W. Zhou, J. Zhang, P. Chen, Q. Pang, L. Zhou, C. Zhou and X. Zhang, *Inorg. Chem. Front.*, 2023, **10**, 511–521.
37 M. H. Fang, K. C. Chen, N. Majewska, T. Leśniewski, S. Mahlik, G. Leniec, S. M. Kaczmarek, C. W. Yang, K. M. Lu, H. S. Sheu and R. S. Liu, *ACS Energy Lett.*, 2020, **6**, 109–114.
38 Y. Xue, Y. Chen, G. Li, W. Xia, Q. Mao, L. Pei, M. Liu, L. Chu and J. Zhong, *Chin. Chem. Lett.*, 2024, **35**, 108447.
39 R. Xiao, N. Guo, C. Jia, Q. Ma, R. Liu and R. Ouyang, *Inorg. Chem.*, 2023, **62**, 9120–9129.
40 S. Su, C. Hu, S. Ding, Y. Sun, L. Sun, Y. Zou, R. Liu, Z. Lei, B. Teng and D. Zhong, *Adv. Opt. Mater.*, 2024, **12**, 2302383.
41 S. Zhao, Z. Mu, L. Lou, S. Yuan, M. Liao, Q. Lin, D. Zhu and F. Wu, *J. Rare Earths*, 2023, **41**, 1895–1903.
42 Q. Zhang, D. Liu, Z. Wang, P. Dang, H. Lian, G. Li and J. Lin, *Adv. Opt. Mater.*, 2023, **11**, 2202478.
43 X. Y. Dai, X. K. Zou, M. K. Wei, X. J. Zhang, B. Dong, X. M. Li, Y. Cong, D. Y. Li, J. Zhao, M. S. Molokeev and B. F. Lei, *Adv. Opt. Mater.*, 2024, **12**, 2401608.
44 X. Zhang, K. Chen, T. Deng, J. Yuan, R. Zhou, T. Yu, Y. Zhou and E. Song, *Mater. Today Chem.*, 2022, **26**, 101194.
45 R. Li, Y. Liu, C. Jin, L. Zhang, J. Zhang, X. J. Wang, G. Chen and J. Jiang, *Laser Photonics Rev.*, 2023, **18**, 2300608.
46 T. T. Deng, E. H. Song, Y. Y. Zhou, L. Y. Wang and Q. Y. Zhang, *J. Mater. Chem. C*, 2017, **5**, 12422–12429.

47 Z. Zhou, G. Ji, Z. Fei, F. He, E. Song, J. Qiu, Z. Yang and G. Dong, *Laser Photonics Rev.*, 2025, 2402099.
48 C. Wang, J. Lin, X. Zhang, H. Dong, M. Wen, S. Zhao, S. Yuan, D. Zhu, F. Wu and Z. Mu, *J. Alloys Compd.*, 2023, **942**, 168893.
49 C. Zhong, Y. Xu, X. Wu, S. Yin, X. Zhang, L. Zhou and H. You, *Adv. Mater.*, 2024, **36**, 2309500.
50 M. Zhao, Y. Y. Zhou, M. S. Molokeev, Q. Y. Zhang, Q. L. Liu and Z. G. Xia, *Adv. Opt. Mater.*, 2019, **7**, 1801631.
51 J. a Lai, W. Shen, J. Qiu, D. Zhou, Z. Long, Y. Yang, K. Zhang, I. Khan and Q. Wang, *J. Am. Ceram. Soc.*, 2020, **103**, 5067–5075.
52 Z. Yang, Y. Zhao, Y. Zhou, J. Qiao, Y. C. Chuang, M. S. Molokeev and Z. Xia, *Adv. Funct. Mater.*, 2022, **32**, 2103927.
53 Z. Wu, J. Xiang, C. Chen, Z. Li, X. Zhou, Y. Jin and C. Guo, *Ceram. Int.*, 2024, **50**, 5242–5249.
54 Q. Lin, Q. Wang, M. Liao, M. Xiong, X. Feng, X. Zhang, H. Dong, D. Zhu, F. Wu and Z. Mu, *ACS Appl. Mater. Interfaces*, 2021, **13**, 18274–18282.
55 D. Liu, G. Li, P. Dang, Q. Zhang, Y. Wei, L. Qiu, H. Lian, M. Shang and J. Lin, *Light: Sci. Appl.*, 2023, **12**, 248.
56 S. Liu, J. Du, Z. Song, C. Ma and Q. Liu, *Light: Sci. Appl.*, 2023, **12**, 181.
57 F. Zhu, Y. Gao, J. Ding, C. Yan and J. Qiu, *Ceram. Int.*, 2023, **49**, 30613–30622.
58 J. Chen, Y. Gao, J. Chen, X. Lu, M. Tan and J. Qiu, *J. Mater. Chem. C*, 2023, **11**, 2217–2228.
59 Y. Zhang, Z. Gao, Y. Li, H. Wang, S. Zhao, Y. Shen, D. Deng and S. Xu, *Ceram. Int.*, 2024, **50**, 31589–31597.
60 Y. Deng, F. Zhu, Y. Gao and J. Qiu, *Inorg. Chem.*, 2024, **63**, 6555–6563.
61 C.-J. Tang, B.-M. Liu, L. Huang, J. Wang and Q. Tang, *J. Mater. Chem. C*, 2022, **10**, 18234–18240.
62 L. Fang, L. Lu, L. Zhang, H. Wu, H. Wu, G. Pan, Z. Hao and J. Zhang, *J. Alloys Compd.*, 2024, **1003**, 175743.
63 F. Zhu, Y. Gao, B. Zhu, L. Huang and J. Qiu, *Chem. Eng. J.*, 2024, **479**, 147568.
64 Y. Liu, C. Dou, F. Dou, Z. Zhang, X. Gao, H. Zhang, S. Wang, X. Wang and H. Jiao, *J. Mater. Chem. C*, 2024, **12**, 13508–13515.
65 X. Lu, Y. Gao, J. Chen, M. Tan and J. Qiu, *ACS Appl. Mater. Interfaces*, 2023, **15**, 39472–39479.
66 F. Zhu, Y. Gao and J. Qiu, *J. Mater. Chem. A*, 2024, **12**, 26929–26938.
67 D. F. Swinehart, *J. Chem. Edu.*, 1962, **39**, 333.